Machine-learning-assisted high-temperature reservoir thermal energy storage optimization

Wencheng Jin [a,*], Trevor A. Atkinson [a], Christine Doughty [b], Ghanashyam Neupane [a],
Nicolas Spycher [b], Travis L. McLing [a], Patrick F. Dobson [b], Robert Smith [c], Robert Podgorney [d]

[a] *Energy and Environment Science and Technology Directorate, Idaho National Laboratory, USA*
[b] *Energy Geosciences Division, Lawrence Berkeley National Laboratory, Berkeley, CA, USA*
[c] *University of Idaho, Moscow, ID, USA*
[d] *Advanced Scientific Computing Division, Idaho National Laboratory, USA*

ARTICLE INFO

ABSTRACT

High-temperature reservoir thermal energy storage (HT-RTES) has the potential to become an indispensable component in achieving the goal of the net-zero carbon economy, given its capability to balance the intermittent nature of renewable energy generation. In this study, a machine-learning-assisted computational framework is presented to identify HT-RTES site with optimal performance metrics by combining physics-based simulation with stochastic hydrogeologic formation and thermal energy storage operation parameters, artificial neural network regression of the simulation data, and genetic algorithm-enabled multi-objective optimization. A doublet well configuration with a layered (aquitard-aquifer-aquitard) generic reservoir is simulated for cases of continuous operation and seasonal-cycle operation scenarios. Neural network-based surrogate models are developed for the two scenarios and applied to generate the Pareto fronts of the HT-RTES performance for four potential HT-RTES sites. The developed Pareto optimal solutions indicate the performance of HT-RTES is operation-scenario (i.e., fluid cycle) and reservoir-site dependent, and the performance metrics have competing effects for a given site and a given fluid cycle. The developed neural network models can be applied to identify suitable sites for HT-RTES, and the proposed framework sheds light on the design of resilient HT-RTES systems.

1. Introduction

The net-zero carbon economy has driven a significant amount of renewable energy production in the United States and around the world. Among the renewable energy resources, wind and solar are the fastest growing sectors, which generate intermittent electricity and further worsen the supply–load imbalance of electric grids. For example, the electricity demand in California increases about 13 GW from noon to night during a typical day, but the solar energy supply diminishes as the demand peaks [1]. The concept of reservoir thermal energy storage (RTES), i.e., injecting hot fluid into a subsurface reservoir and recovering the geothermal energy later, can be used to address the issue of imbalance in supply and load because of its grid-scale storage capacity and dispatchable nature [2]. Note aquifer/geological thermal energy storage (ATES/GeoTES) are other names for RTES, which uses a permeable formation to store thermal fluid, while borehole thermal energy storage (BTES) uses closed pipelines to store thermal fluid, with heat transfer to the surrounding formation by thermal conduction.

RTES can be categorized into low-temperature (LT) and high-temperature (HT) according to the temperature of the injection fluid. The threshold to distinguish LT-RTES from HT-RTES is variously defined as 30 °C in [3,4], 40 °C in [5], and 50 °C in [6]. The majority of the RTES applications around the world are operated at low temperatures and make use of the stored geothermal energy for space heating and cooling [4,5]. The earliest RTES application dates back to 1965 in Shanghai, where several textile factories started to store winter cold water for summer cooling [7]. For HT-RTES, in-situ experiments [8,9], numerical simulations [3,4,10–12], and pilot plant planning [13–15] have been carried out in the last few decades to address the technical challenges and to predict the performance of RTES. One of the extensively investigated RTES performance parameters is the heat recovery efficiency, which is generally defined as the ratio of enthalpy extracted over enthalpy injected during an injection–storage–extraction cycle. Centered on the recovery efficiency, research and development in literature can be grouped into two categories: (1) RTES potential site identification through the calculation of a

---

dimensionless number (e.g., Rayleigh number), which is formulated in terms of geologic formation characteristics and determines recovery efficiency [4,11,16]; and (2) RTES site operation optimization with fixed formation characteristics to maximize recovery efficiency [17–19]. The methodology of treating recovery efficiency as the RTES sole design factor has led to many failures of HT-RTES around the world, as reviewed by Fleuchaus et al. [20]. Because thermal energy supply and demand fluctuate over time, achieving maximum recovery efficiency with a non-optimized dynamic operation is challenging. Identifying suitable sites for HT-RTES has to consider all the performance metrics (e.g., charging/operating time, thermal recovery factor, etc.) and its resilience to operational uncertainty [21].

RTES site identification with resilience consideration requires examining numerous sites with different formation characteristics and to test different operation conditions for each site. The high computational cost of the physical modeling and the time cost associated with pre- and post-processing hinder stakeholders from investing in RTES as they need fast evaluation and may not have access to supercomputers. To alleviate such problems, a simple, robust, and efficient model is usually deduced from the regression analysis of the stochastic data sets [22]. As identified by Bergen et al. [23], machine learning is one of the most effective tools for regression (i.e., surrogate model development), geoscience discovery and geoengineering. The application of machine learning in subsurface energy engineering has increased exponentially in recent years. Examples of these applications include support vector/random forests-enabled main flow pathways identification from a discrete fracture network [24,25], convolutional neural network-enabled parameter determination from images [26,27], and artificial neural network-enabled modeling acceleration [28–30]. More recently, artificial neural networks have been applied for RTES to connect formation characteristics and operating conditions to performance metrics [22]. These authors applied the neural network model to optimize each of the performance metrics (i.e., objectives). However, finding optimal solutions for all objectives simultaneously is not always guaranteed because conflicts exist between these objectives. For example, maximizing the recovery efficiency may lead to decreasing operation time in each cycle. This is because the fast charge and drain of the RTES can lead to a better recovery efficiency. In addition, operations may have other constraints as described previously. Consequently, an effective, fast, and stable workflow to co-optimize HT-RTES performance metrics is needed for HT-RTES site identification and design with the consideration of resilience.

In this effort, we propose a workflow to identify HT-RTES sites with co-optimal performance metrics (i.e., recovery efficiency, charging time, operating time, storage capacity) for electricity generation as shown in Fig. 1. We first introduce the governing equations of the heat-transfer and fluid flow processes involved in HT-RTES, and we develop a generic reservoir model with two operational scenarios: continuous operation and seasonal cycle operation. Powered by the stochastic module in our simulation package, we perform stochastic simulation with formation characteristics and operation conditions sampled from their corresponding distributions using the Monte Carlo method. The successful simulation cases connecting input variables and reasonable performance outcomes constitute a data set, which is then used to train and validate artificial neural network models. The architecture of the neural network models are tuned using the Bayesian optimization algorithm, and those yielding the best prediction performance are chosen as our surrogate models. The surrogate models are coupled to a genetic algorithm to generate the Pareto fronts (i.e., optimal solutions) considering multiple objective functions for four identified potential sites. Discussion of the results and conclusions of the proposed methodology are then summarized. The proposed workflow can quickly screen potential sites with the consideration of multiple HT-RTES performance metrics instead of relying solely on recovery efficiency, which would help stakeholders make resilient decisions in the early stages of RTES investment.
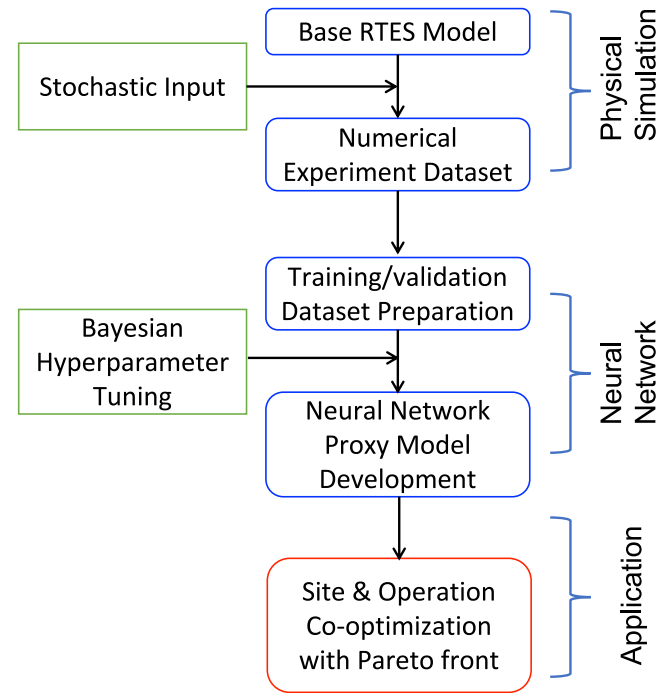

Fig. 1. Workflow of the proposed optimization framework.

2. Methodology

2.1. Governing equations

For the generic simulation, the following assumptions are made:

- Formation is fully saturated with a single phase fluid;
- Formation is homogeneous with isotropic properties;
- Pores are not compressible and not expandable (i.e., constant porosity);
- The geomechanics and geochemical effects on the RTES are not significant;

With these assumptions, fluid flow and heat transfer in porous media can be governed by the conservation of mass and energy in terms of pore pressure $P(Pa)$ and temperature $T(K)$ as:

$$\frac{\phi}{K_f}\frac{\partial P}{\partial t} + \phi\alpha_f\frac{\partial T}{\partial t} - \nabla \cdot \frac{\kappa}{\mu}(\nabla P - \rho_f g) - q/\rho_f = 0 \tag{1}$$

$$\frac{\partial \epsilon}{\partial t} - \nabla \cdot \lambda\nabla T - \nabla \cdot \left[\rho_f C_f T\frac{\kappa}{\mu}(\nabla P - \rho_f g)\right] = 0 \tag{2}$$

where q (kg/m^3/s) is the fluid source/sink, $\phi(-)$ is the formation porosity, K_f (Pa) and α_f (1/K) are the bulk modulus and the volumetric thermal expansion coefficient of the fluid, respectively. κ (m^2) denotes the formation isotropic permeability, and μ (Pa s) represents the fluid viscosity. The vector g (m/s^2) stands for the gravity, and ϵ (J/m^3) is the energy density for the fluid–matrix system. It is calculated as:

$$\epsilon = (1 - \phi)\rho_m C_m T + \phi\rho_f C_f T \tag{3}$$

in which ρ_β (kg/m^3), C_β (J/kg/K) represents the density and the specific heat of the substance β ($\beta = m$: matrix, $\beta = f$: fluid), respectively. λ (W/m/K) in Eq. (2) is the thermal conductivity. Note that the constitutive equation of Darcy's law is embedded in the two governing equations.

We solve the above governing equations using the FALCON (Fracturing And Liquid CONvection [31,32]) code, which is built upon the open-source finite element package MOOSE (Multiphysics Object Oriented Simulations Environment) [33]. For thermo-hydraulic problems,
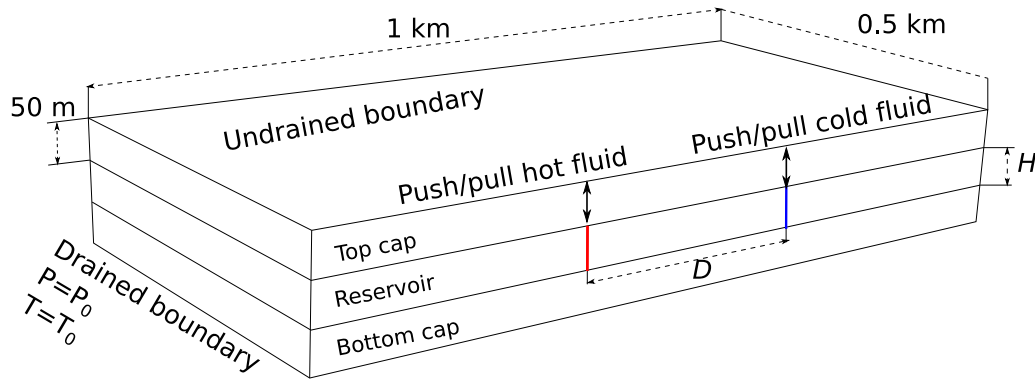
Fig. 2. Geometry and boundary conditions of the generic formation with doublet system for simulation.

validation of the solver has been conducted by comparing numerical prediction against field measurement [9] at Auburn University [19] and by comparing predictions against previous studies [4,11].

2.2. Generic reservoir model

A generic reservoir formation confined by low permeability caprock (e.g., shale) at the top and bottom shown in Fig. 2 is used for the numerical simulations. We fix the caprock with 50 m thickness as a preliminary study indicates that the heat front in the caprock does not exceed 50 m for 10 years of operation, which is the maximum time considered in this study. The reservoir thickness varies from 10–100 meters with 10-meter intervals. To minimize the influence of boundary conditions and the computational cost, the domain is fixed at 1000 meters in the two horizontal directions. The most common doublet well configuration is selected in this study, and we further constrain the simulation domain with symmetry shown in Fig. 2. All the side surfaces are maintained constant at their initial pore pressure $P = P_0$ and temperature $T = T_0$, except the symmetrical surface, which is fixed with a no-flux boundary. We consider that the caprock and the bedrock with extremely low permeability prevents heat and fluid exchange, and we apply undrained conditions for the top and bottom surfaces of the domain. For the 10 simulation domains with different reservoir thicknesses, we mesh the domain using hexahedron-shaped elements with sizes ranging from 5 meters along the symmetrical surface to 50 meters at the boundary surfaces. Mesh sensitivity analysis was carried out for the 10-meter thickness reservoir case, showing insignificant variation in the RTES performance.

Table 1 shows the values of the physical properties and the operating conditions used for the RTES simulations. The caprock properties are fixed with typical values of shale [34,35]. For the reservoir, all parameters have a min–max value range corresponding to a typical sandstone formation [36,37], except for the grain density and the specific heat which are fixed given that they do not have a wide physical range. We identified three operation parameters, i.e., the doublet well distance D, the injection fluid temperature T_i, and the injection flow rate Q. All these value ranges are picked to achieve high-temperature grid-scale RTES. The initial temperature and pore pressure for each simulation case are not stochastically sampled from distributions; instead, they are implicitly related to the depth of the reservoir. Following Zhang [38] and Dowdle and Dobb [39], we use the following equations to assign uniform initial temperature T_0 and initial pore pressure P_0 in terms of depth Z:

$$P_0(Z) = \begin{cases} \rho_f g Z, & Z < 2000 \\ \rho_f g Z + (Z - 2000)\rho_f g, & Z \geq 2000 \end{cases} \quad (4)$$

$$T_0(Z) = 26.67 + 0.02005Z \quad (5)$$

We use the equation of state of water & steam in IAPWS-97 [40] to govern the physical properties of the working fluid including fluid

Table 1
Modeling parameters with uncertain/fixed values used for the simulations.

Parameters	Symbol	Units	Values	
			Reservoir	Caprock
Permeability	κ	m²	$10^{-15} - 10^{-11}$	10^{-18}
Porosity	ϕ	–	$0.01 - 0.30$	0.01
Themal Conductivity	λ	W/(m K)	$2.0 - 4.0$	2.5
Specific Heat	C_m	J/(kg K)	930	1000
Grain Density	ρ_m	kg/m³	2650	2500
Formation Thickness	H	m	10–100	50
Well Distance	D	m	100–200	
Flow Rate	Q	kg/s	1–1000	
Inj. Temperature	T_i	°C	100–300	
Formation Depth	Z	m	1000–3000	

density ρ_f, viscosity μ, and specific heat C_f (Eqs. (1) & (2)), all of which are dependent on the fluid pressure and temperature. As demonstrated by Sheldon et al. [4], simplification of those state equations with simple linear and exponential functions leads to inaccurate simulation results.

2.2.1. Continuous operation

We investigate two operational scenarios to evaluate the performance of HT-RTES for addressing two practical issues: (1) continuous electricity generation when other energy supplies are affected by extreme weather (e.g., 2021 US Texas record cold); (2) mitigation of the seasonal imbalance of energy supply and demand. For the first scenario, we operate the RTES by charging the system followed by discharging for electricity generation. During the charging time, cold fluid is extracted from the cold well and heated to a fixed temperature, then re-injected into the reservoir through the hot well at the same rate as the extraction. The same injection and extraction rates ensure the pore pressure disturbance in the reservoir is minimized. The charging time lasts until the thermal front reaches the cold well, at which time the temperature of the extracted fluid starts to exceed the initial reservoir temperature T_0. At the end of the charging time, fluid is extracted from the hot well for the generation of electricity with the post-generation energy-depleted fluid being injected back into the reservoir through the cold well. The extraction and injection rates during the discharging period also remain the same as the charging time, and the injected fluid temperature into the cold well is the same as the initial reservoir temperature. It is important to note that high-temperature RTES is targeted to generate electricity when thermal energy is extracted. The energy extraction period is terminated when the temperature of the extracted hot well fluid is reduced by 20% in relation to the difference between the fluid injection temperature and the initial reservoir temperature, i.e., we stop discharging when the temperature of the hot well T_{hot} satisfies $(T_{hot} - T_0)/(T_i - T_0) < 80\%$. This high cut-off temperature is adopted to ensure the extracted hot fluid can be used for electricity generation.
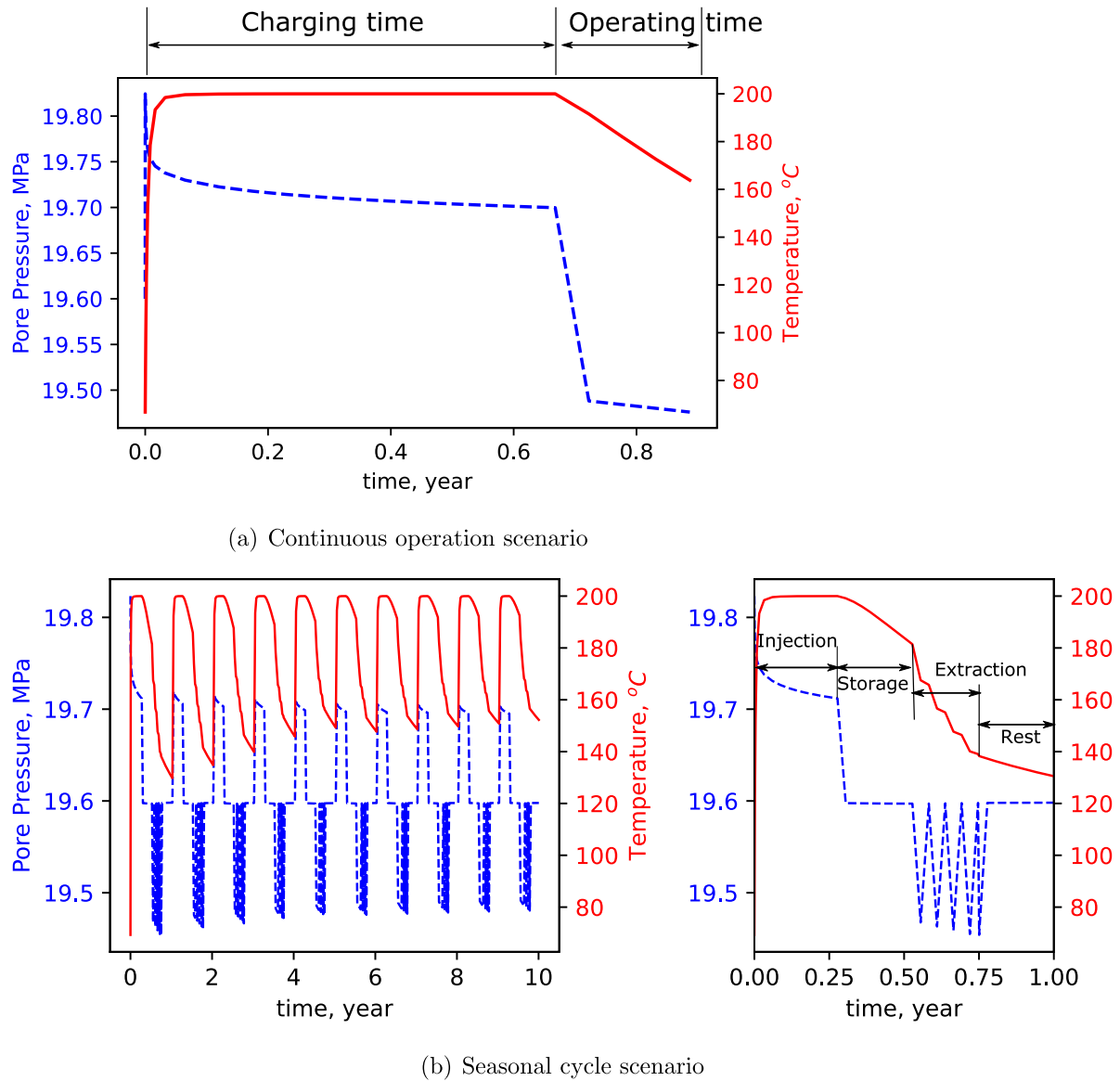
(a) Continuous operation scenario

(b) Seasonal cycle scenario

Fig. 3. Demonstration of the two considered operational scenarios: (a) Pore pressure and temperature evolution at the middle of the hot well for the continuous operation scenario; (b) Pore pressure and temperature evolution at the middle of the hot well for the scenario of injection–storage–extraction–rest seasonal cycle of 10 years operation. Note that the extraction operation only occurs when the temperature of the fluid in the hot well (T_{hot}) exceeds the cut-off temperature (i.e., $(T_{hot} - T_0)/(T_i - T_0) \geq 80\%$), and the hot well temperature can raise again due to heat conduction when extraction stops. This temperature raise will restart the extraction which results in a zigzag-shaped curve during the extraction season as shown above. Note the temperature of the extracted fluid from the hot well has a discrepancy with the temperature at the middle of the well.

Fig. 3(a) demonstrates the operation as stated above for the simulation case with a reservoir thickness $H = 50$ m at the depth $Z = 2000$ m, which results in initial reservoir pore pressure $P_0 = 19.6$ MPa, and initial temperature $T_0 = 66.7°C$ following Eqs. (4)–(5). The rest of the formation properties are $\kappa = 10^{-12}$ m^2, $n = 0.01$, $\lambda = 2$ W/(m K). The operation conditions are $Q = 10^{1.5}$ kg/s, $D = 200$ m, and $T_i = 200$ °C. With these specifics, the reservoir is fully charged after 0.71 years of continuous injection. The operating time lasts about 0.23 years as the fluid extracted from the hot well drops to 173 °C. Note the two wells penetrate the whole formation thickness as shown in Fig. 2, and the wells are realized by line sinks to inject/extract fluid to/from the system. The pore pressure shown in Fig. 3(a) is sampled from the node close to the middle of the hot well, and the initial spike results from the way the boundary condition is applied and the reduction of viscosity induced by the sudden increase of fluid temperature. Its value gradually reduces to quasi-equilibrium (19.70 MPa). If a physical well is simulated, the pore pressure spike at the well will not be shown,

and the pore pressure evolution in the well will gradually reach a plateau with a value equal to the value in Fig. 3(a). This simplified well realization will not have any influence on the RTES performance as the reservoir is assumed homogeneous. But it greatly facilitates stochastic simulation as the wells can be placed anywhere without remeshing. This is also the reason why the temperature at the middle of hot well is not exactly 173 °C when the operation ends. Fig. 4(a) shows the heated region for the demonstration case at the end of charging time $t = 0.71$ year and operating time $t = 0.94$ year. The buoyancy effect is clearly shown. i.e., injected hot fluid is less dense compared to the initial reservoir fluid, and it rises buoyantly upwards to the caprock. The heated volume is asymmetrical with respect to the hot well because the extraction of the cold well speeds up the fluid flow in the direction towards the cold well. After the operating time, there is still a significant amount of hot fluid remaining in the reservoir. In addition to the charging time T_c and the operating time T_o, we calculate the energy recovery efficiency R and the storage capacity E as the other
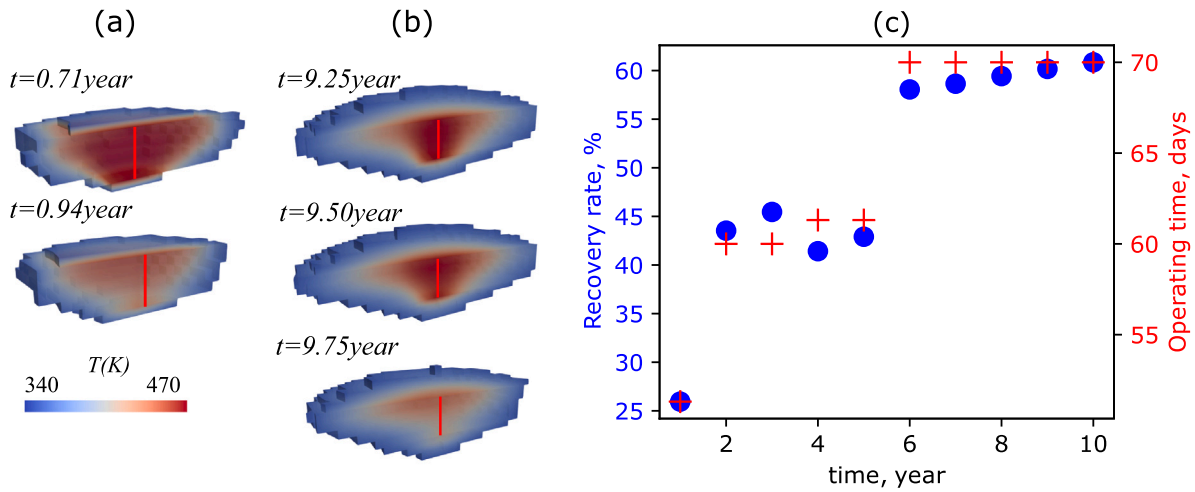
Fig. 4. Temperature distribution of the heated volume in the doublet system for the continuous operation scenario (a) at the end of the charging time (t = 0.71 year) and at the end of the operating time (t = 0.94 year), and for the seasonal cycle scenario (b) at the end of the injection, storage and extraction of the 10th operating year. The hot well is denoted as a red line and the cold well is outside of the domain shown in the figure. (c) The calculated annual recovery efficiency and annual operating time for the seasonal cycle case.

two RTES performance metrics, they are defined as

$$R = \frac{\int_{T_o} QC_f(T_{hot} - T_{cold})dt}{\int_{T_c} QC_f(T_{hot} - T_{cold})dt} \quad (6)$$

$$E = \int_{T_c} QC_f(T_{hot} - T_{cold})dt \quad (7)$$

where Q is the injection/extraction mass flow rate [kg/m], C_f is the specific heat of the fluid [J/kg K], which is a function of fluid temperature and pressure. T_{hot} and T_{cold} are the temperature of the injected hot fluid (constant during T_c) or extracted hot fluid in the hot well, and the temperature of the injected cold fluid (constant during T_o) or extracted cold fluid from the cold well shown in Fig. 2. This definition replaces the reference temperature of the conventional single-well push-pull model recovery efficiency calculation [11,41], because the doublet system uses formation fluid as the working fluid.

A stochastic module has been recently developed in the MOOSE framework, which can automatically launch a large number of simulations with input parameters sampled from given distributions. Here, using the Monte Carlo method, we use this feature to perform stochastic simulations with operating conditions and formation characteristics sampled from their uniform distributions (Table 1). Given the several orders of magnitude range of permeability and injection flow rate, the utilization of uniform distributions with their min–max values can result in insufficient samples in the range close to the lower end. We, instead, use the uniform distributions of their log-scale (i.e., $\log(Q)$ and $\log(\kappa)$). Fig. 5 shows the histograms of the input parameters and their corresponding output parameters from all of the realized simulations. All of these simulations are screened by the Theis theory [42] to avoid hydrofracturing the formation, i.e., the high injection rate induced stress exceeds the sum of the effective in-situ stress and the tensile strength of the formation and creates fractures in the formation. This strategy is also adopted by Sheldon et al. in their HT-RTES analysis [4].

In addition to avoiding hydrofracturing the formation, we also screened out the cases that are non-reasonable in practice (e.g., charging time exceeds 10 years) and violate the assumptions in Section 2.1 (e.g., high injection temperature at low pore pressure formation results in fluid vaporization). As shown in Fig. 5(a), all those excluded cases result in non-uniform distributions of flow rate and permeability. Each of the realized RTES simulations generates its corresponding performance metrics defined previously, i.e., thermal energy recovery efficiency, the time needed to fully charge the RTES (charging time), the time that RTES can continuously generate electricity after fully charged (operating time), and the storage capacity. All four performance metrics

have a close to power-law distribution except the recovery efficiency, and their min–max ranges cross several magnitudes. To differentiate the performance metrics data with small magnitude, we plotted them in a logarithmic scale as shown in Fig. 5(b) except recovery efficiency. The logarithmic handling of a dataset has a huge influence on the accuracy of neural network model training and validation, as discussed in Section 4.

2.2.2. Seasonal cycles

For the second scenario, we use the well-established seasonal injection–storage–extraction–rest cycle operation. As demonstrated in Fig. 3(b), we charge the reservoir during the summer season when the energy supply surpasses demand followed by the fall season storage. Note all the formation parameters and operating conditions are the same as the continuous operation case. In the winter, hot fluid is extracted from the hot well to generate electricity. Similar to the previous case, extraction is terminated once the extracted fluid T satisfies $(T - T_0)/(T_i - T_0) < 80\%$. However, we note the hot well temperature may rise again due to heat convection following the end of extraction, so the extraction is restarted once the fluid temperature in the hot well T reaches $(T - T_0)/(T_i - T_0) \geq 80\%$. This stop–restart cycle determined by the hot well fluid temperature continues throughout the winter season shown as the zigzag curve section in Fig. 3(b). The total amount of time used to generate electricity in the winter is labeled as operating time, which constitutes one of the RTES performance metrics. We note the influence of time-step size on the operating time is insignificant. In the spring season, we stop operation to rest the RTES system.

As shown in Fig. 3(b), we simulate 10 years for the seasonal cycle scenario of each case. The pore pressure evolution sampled from a node close to the middle of the hot well shows spikes at the start of injection of each summer, which is similar to the previous case resulting from the line sink boundary condition and fluid viscosity dropping with increasing temperature. This effect is less significant over time because the RTES system has been warmed up as a portion of thermal energy is not extracted during the winter in each cycle. The warming trend is clearly shown in Fig. 3(b) as the temperature at the end of each cycle continues to increase throughout the 10 years of operation. This phenomenon is further demonstrated in Fig. 4(b), heat convection at the storage season (i.e., fall) slightly increases the heat front (t = 9.5 year). Yet, the buoyancy effect and the temperature cut-off leave a significant amount of thermal energy in the system after extraction (t = 9.75 year). Fig. 4(c) plots the evolution of operating time and energy recovery efficiency over the 10 years of operation. Only about
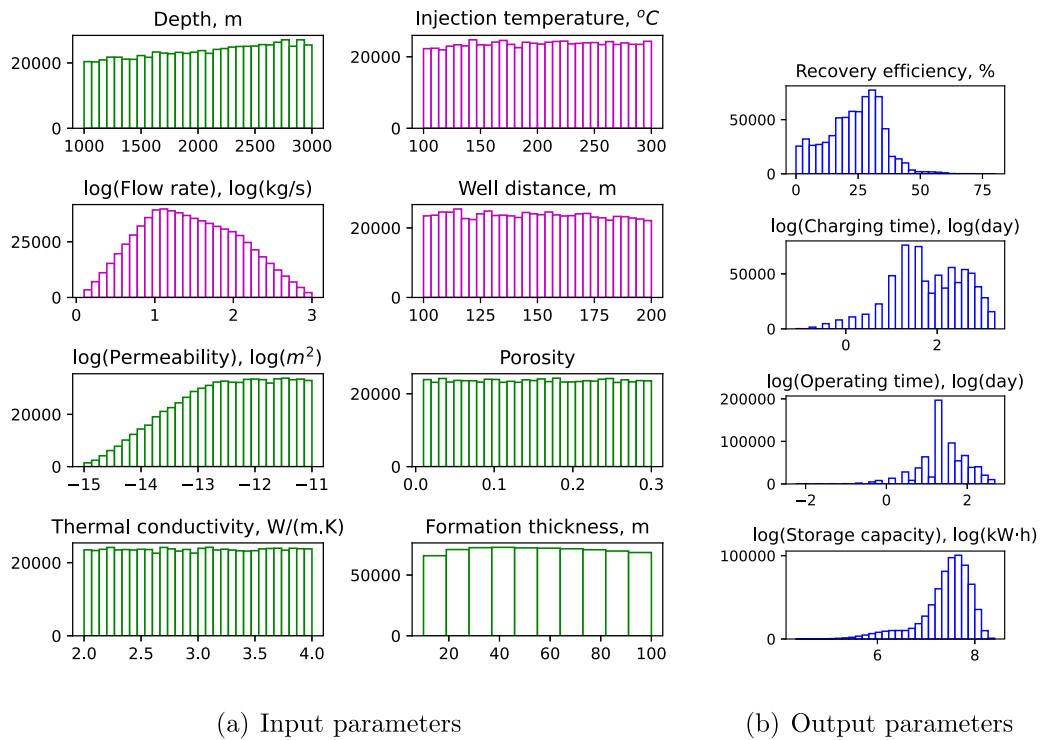
(a) Input parameters

(b) Output parameters

Fig. 5. Histograms of the input and output parameters for all the realized simulations of continuous operation. The *y*-axis stands for the realized simulation numbers after screening. (a) Formation characteristics are color-coded in green and operation conditions are color-coded in magenta. Note for the cross-magnitude flow rate and permeability, we use exponent to assign the min–max values of their uniform distribution range. (b) The output parameters color-coded in blue include all four RTES performance metrics: recovery efficiency, charging time, operating time, and storage capacity. Note all the realized simulations exclude physically meaningless cases (e.g., fracturing the formation with high injection rate and low permeability) and non-reasonable cases (e.g., over 10 years of charging time).

25% of the stored thermal energy is recovered in 50 days of the winter season in the first year. Yet, the numbers increase to 60% of recovery efficiency over 70 days of operating time in the 10th year. Note large increase from year 1 to year 2 and from year 4 to year 6 in Fig. 4(c) is a result of the well temperature detection with respect to the cut-off temperature. This non-smooth increase does not affect the performance quantities, i.e.: the average annual energy recovery efficiency $\bar{R}$ and the average annual operating time $\bar{T}_o$ over the 10 years of operation. We also calculate the annual storage capacity (i.e., the annual total thermal energy injected into the system $\bar{E}$) to measure the RTES performance. We use Eq. (6) to calculate the recovery efficiency.

We use the same methodology detailed in the previous scenario to carry out the Monte Carlo stochastic simulation for the seasonal cycle case. Fig. 6(a) shows the histograms of the formation parameters (green) and the operating conditions (magenta) of all the realized simulations. The screening-out process of the physically meaningless cases and the unreasonable cases in practice also results in the non-uniform distribution in flow rate and permeability, which are the same as the continuous operation scenario. The non-uniform distribution in formation thickness is because a large number simulations with large formation thickness (i.e., $H =90$ m, 100 m) could not complete 10 years of simulation within the maximum wall time of the HPC cluster. We argue that the missing piece of data only accounts for about 10% of the total data, which will not influence the overall trend in the following data analysis. Fig. 6(b) plots the histograms of the RTES performance metrics for the seasonal cycle case. Because we stop and restart the extraction process during the winter season according to the fluid temperature in the hot well, the recovery efficiency is higher than the previous case, and the operation time spans from 50 days to 80 days with a close to uniform distribution. The predicted annual storage capacity is still close to a power-law distribution, and we plotted it in the logarithmic scale similar to the continuous operation case. Note the charging time in the seasonal cycle operation is a constant (i.e., 3 months), and it is not a performance indicator.

Comparing the performance metrics of the two operating scenarios in Fig. 5(b) and Fig. 6(b), the continuous operation has about a factor of two lower recovery efficiency and one magnitude higher energy storage than the seasonal cycle. The low recovery efficiency is because of the higher thermal energy loss to the formation for a comparatively long time of one-time injection and extraction and the high cut-off temperature during the extraction stage. Also, for the seasonal cycle, the extraction stops and restarts several times during the extraction season according to the temperature inside the hot well, which helps to recover more energy. We note the storage capacity in the continuous operation is defined as the total amount of energy injected when the thermal front reaches the cold well. While the annual storage in the seasonal cycle is the injected energy in the fixed three-month time frame. The continuous operation is designed for handling extreme weather. In practice, the charging process is more likely to be discontinuous and the extraction may start any time before the system is fully charged. This dynamic operation can have a huge influence on the recovery efficiency, and the continuous operation is an extreme case of all possible scenarios.

2.3. Neural networks training

The approaches used to generate a reduced-order model from the above physics simulations range from the simple linear least square method to the sophisticated artificial neural network (ANN) method. We use the ANN to build reduced-order models (also called meta-models and surrogate models) for correlating the input parameters and the RTES performance metrics. A typical ANN resembles the interconnected networks of biological neurons in the brain, as demonstrated in Fig. 7. ANN neurons are presented by nodes associated with an activation function (f). A group of neurons with a specific number and the same activation function constitute an ANN layer, and each neuron in the layer takes the weighted sum of the output of neurons
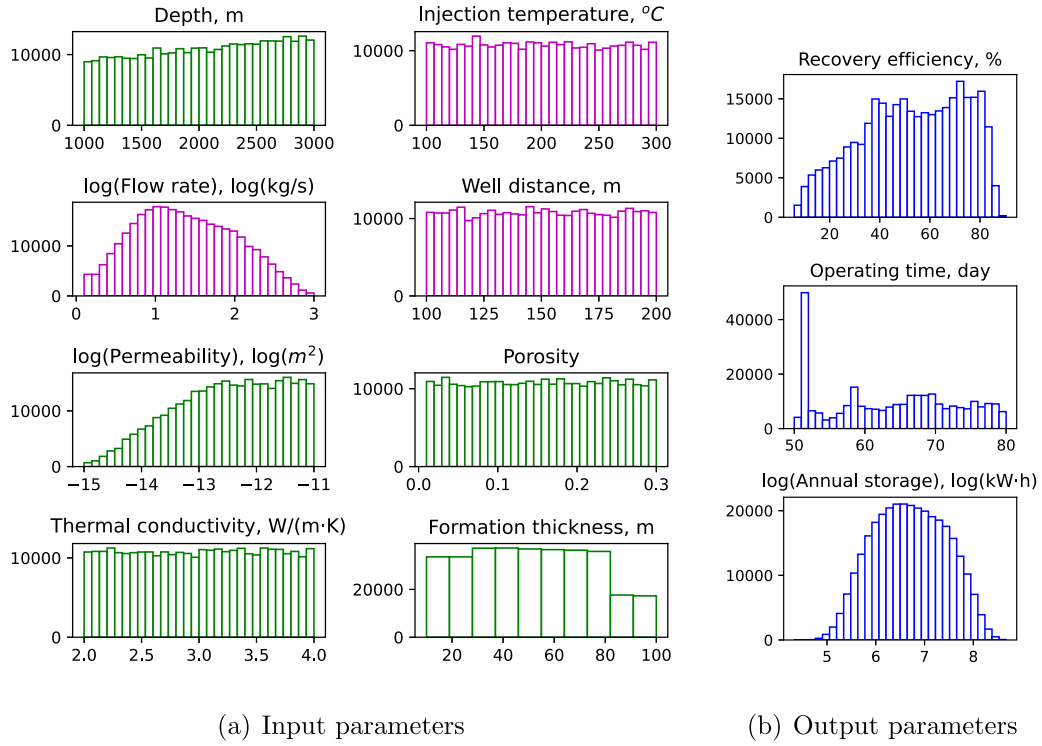
Fig. 6. Histograms of the input and output parameters for all the realized simulations of the seasonal cycle operation. The *y*-axis stands for the realized simulation numbers after screening. Similar to the previous operation, we color-code the formation characteristics in green, the operation conditions in magenta, and the performance metrics in blue. Note the performance metrics are all annual average values.
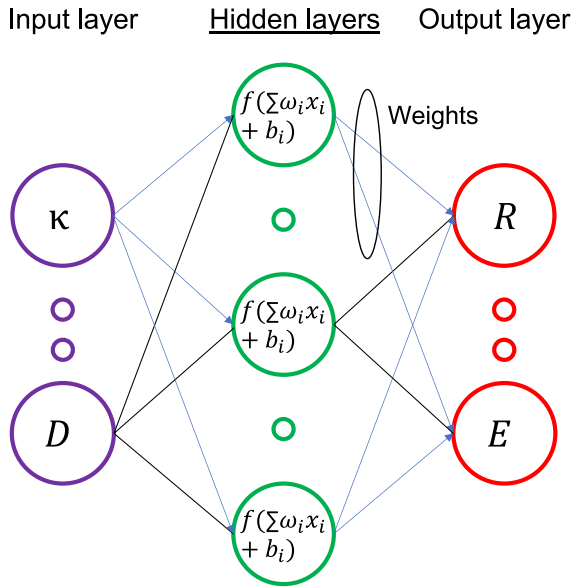

Fig. 7. Structure of a typical deep multi-layer neural network model.

Table 2
The search space for optimizing neural network architecture.

Hyperparameters	Value range
Number of hidden layers	1–5
Number of neurons in each layer	100–500 (step 20)
Activation function	Relu, Linear, Sigmoid

The first layer that takes the input data is called the input layer, and here has 8 neurons of formation characteristics (i.e., Z, κ, n, λ, and H) and operating conditions (i.e., D, T_i, and Q). The last layer is called the output layer, which has 4 neurons for the continuous operation and 3 neurons for the seasonal cycle operation corresponding to their performance metrics.

The performance of an ANN strongly depends on its architecture, i.e., the number of hidden layers, the number of neurons for each hidden layer, and the activation functions for each layer. These parameters are called hyper-parameters in data science, and the process of getting the best ANN architecture is called hyper-parameter tuning. In this paper, we use the well-established Bayesian optimization algorithm [43] to find the optimal architectures of neural networks for the two data sets (i.e., the input and output parameters of the two operation scenarios in Figs. 5 and 6). The Bayesian optimization algorithm constructs a probabilistic function mapping from hyper-parameter spaces to its objective, which is defined as the minimum mean absolute error between the physical simulation results and the ANN predictions. The probabilistic function is iteratively updated by comparing the optimal configuration from the previous evaluation and the current configuration, and the iteration stops when the objective is met. Table 2 defines the searching spaces of the hyperparameters in ANN architecture design. Note that we used a linear function (Linear) and a rectified linear function (Relu), which does and does not allow backward propagation, respectively. The Sigmoid logistic function is also used to restrain the outputs in physically reasonable ranges. The

in the previous layer as its input, makes a prediction according to the activation function and passes the prediction to the next layer. Mathematically,

$$y = f\left(\sum_i^N \omega_i x_i + b_i\right) \tag{8}$$

where x, y, ω, and b represent input, output, weight and bias, respectively. N is the total number of inputs, which is equal to the total number of neurons of the previous layer if neuron drop is not activated.

step in the space of neuron numbers is used to reduce the computational cost.

We use the TensorFlow machine learning platform for ANN architecture training and optimization. Following the standard procedure, we first normalize the input and the output variables using their corresponding mix-max values. Note the charging time, operating time, and storage capacity of the continuous operation and the annual storage of the seasonal cycle were logarithmically scaled. This scaling step speeds up the ANN training process and their performance, as all the numbers passing through neuron layers are limited and balanced in the same small range. We then randomly divide the scaled data into three sets with 80% for training, 10% for validation, and 10% for testing. The training set constitutes all the characteristics of the physical process, and it enables the ANN model to capture all those characteristics through training. The ANN training is the process of obtaining unique values of the weight ω and the bias b (Eq. (8)) to minimize a cost/objective function, which is defined the same as for the hyper-parameter tuning objective function. A specified number of randomly chosen samples of the training data set is used to calculate the ANN model prediction, the cost function value, and the gradient of ANN model parameters following the stochastic gradient descent method (i.e., adam [44]) for each iteration, and the iteration stops when the full training data is exhausted. This full iteration cycle is also termed an epoch, and the ANN parameters are then updated using the calculated gradients for each ANN parameter. A typical ANN training process constitutes many epochs until the cost function meets the specific limit. We use 300 epochs in this paper. At the end of the epoch, we expose the validation data set to the current ANN model for performance evaluation and to avoid over-fitting. Over-fitting is shown as a very small error in training samples, yet, the ANN cannot predict accurately for the other general cases, such as a sample in the validation set. We prevent over-fitting by terminating the training process when the performance of the ANN model does not improve for 20 continuous epoch training cycles. When the whole epoch training is completed, we test the performance of the well-trained ANN model by evaluating the performance of the testing data set.

2.4. Genetic algorithm for multi-objective optimization

The optimization of the RTES performance system is an multi-objective co-optimization problem. Mathematically, we can express it as

$$\max(E, R, T_o, -T_c)$$
$$\text{s.t.} \quad -15 \leq \log(\kappa) \leq -11, \quad 0.01 \leq n \leq 0.3, \quad 2 \leq \lambda \leq 4$$
$$10 \leq H \leq 100, \quad 100 \leq D \leq 200, \quad 0.1 \leq \log(Q) \leq 3 \tag{9}$$
$$100 \leq T_i \leq 300, \quad 1000 \leq Z \leq 3000$$

Note the minus sign for charging time (T_c) is used to minimize its value. Because the RTES performance metrics may have dependent or conflicting relationships, the solution of the above problem is not unique, and all the solutions constitute the Pareto front. For example, the optimal solution for recovery efficiency (R) may give the worst operating time T_o, while increasing charging time T_c results in increased operating time T_o. The mathematical explanation of the Pareto front can be shown as follows:

$$P = \{x^* \in \Omega | \neg \exists x_k \in \Omega : x_k \prec x^*\} \tag{10}$$

where x^* are the solutions belong to the Pareto front, and x_k denote all possible solutions to the problem. $\prec$ represents dominance. For the maximization problem of this paper, solution x_1 dominating solution x_2 can be mathematically expressed as

$$\forall i \in 1, 2, \ldots, N : f_i(x_1) \leq f_i(x_2),$$
$$\exists j \in 1, 2, \ldots, N : f_j(x_1) < f_j(x_2). \tag{11}$$

Given the multi-objective optimization problems only constrained by the ranges of searching variables, we adopt genetic algorithms (GAs)

Table 3
Summary of the optimal neural network architectures for the two investigated operational scenarios. Note Relu stands a rectified linear function.

Layer	Continuous Operation		Seasonal Cycle	
	Neurons	Activation	Neurons	Activation
Input	160	Linear	120	Linear
Dense-1	500	Relu	280	Relu
Dense-2	500	Linear	260	Relu
Dense-3	500	Linear	480	Relu
Dense-4	500	Sigmoid	160	Sigmoid
Output	4	–	3	–

to obtain the Pareto fronts. The GA is a stochastic search method that mimics the process of biological evolution. The algorithm creates the first generation of the population by a fixed number of random realizations in the search space. Then, individuals in the population are mutated, crossed over, and selected in each generation. The selection process is governed by the fitness (objective) functions, and only the selected individuals are passed to the next generation until the convergence is satisfied or the maximum generation is reached. In this paper, we use the open-source python library Geatpy [45] with various genetic algorithms implemented, to search the Pareto front. Specifically, the non-dominated sorting genetic algorithm II (NSGA-II) [46] is used with 200 initial populations and 100 maximum generations.

3. Results
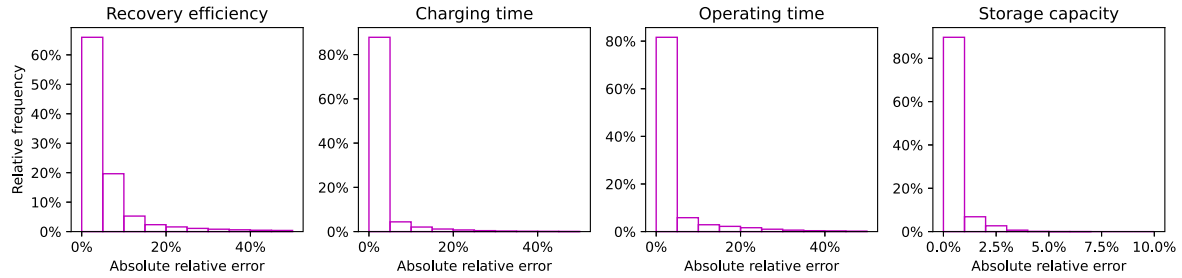
3.1. Neural networks validation

Table 3 summarizes the architecture of the best ANN models optimized from the Bayesian algorithm detailed in Section 2.3. The hyper-parameters vary from each other for the two operational scenarios, indicating the difference in the characteristics of the training data.

Fig. 8 shows the cross-validation of the trained ANN models for the two operational scenarios. For the continuous operation case in Fig. 8(a), the ANN predicted results agree with the physics-based simulation results better for charging time, operating time, and storage capacity than for recovery efficiency. This is because the relationship between the recovery efficiency and the input variables (formation characteristics and operating conditions) is highly nonlinear, and the ANN model cannot capture all the features. This is reflected by the recent work [4] that shows the recovery efficiency is highly nonlinear in terms of formation thickness and the modified Rayleigh number. Similarly, the cross-validation of the ANN prediction against the testing data set of the physics-based simulations for the seasonal cycle case is shown in Fig. 8(c). Compared to the continuous operation case (Fig. 8(a)), the ANN prediction is excellent for all RTES performance metrics, which indicates that all important features of training data sets are captured by the ANN model. This is because the performance metrics of the continuous operation have a more complex nonlinear relationship with respect to the stochastic variables. For example, the storage capacity for the continuous operation depends on all stochastic input, while the annual storage of the seasonal cycle only depends on injection rate and injection temperature. A sophisticated ANN model with more features (e.g., deeper layers, non-zero dropping rates) is needed to better surrogate the physics simulations of the continuous operation.

We adopted the absolute relative error $error_i = |T_i - Y_i|/T_i$ to quantify the performance of the trained ANN models, where T_i is the targeted true value of the RTES performance metrics from the physical simulation, while Y_i is the ANN prediction. Figs. 8(b) and 8(d) show the histograms of the absolute relative error of the performance metrics for the two operations. For the continuous operation, about $65\%, 85\%, 80\%,$ and 85% of all test data have an error less than $5\%, 5\%, 5\%,$ and 1% for the recovery efficiency, charging time, operating time, and storage capacity, respectively. The averages of the absolute relative error
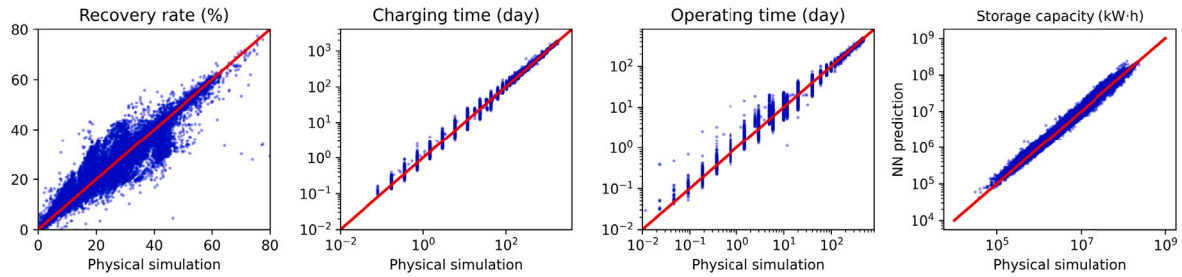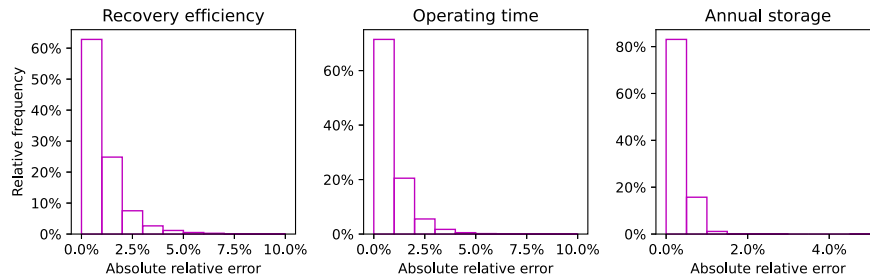
(a) Continuous operation scenario - cross validation

(b) Continuous operation scenario - relative error
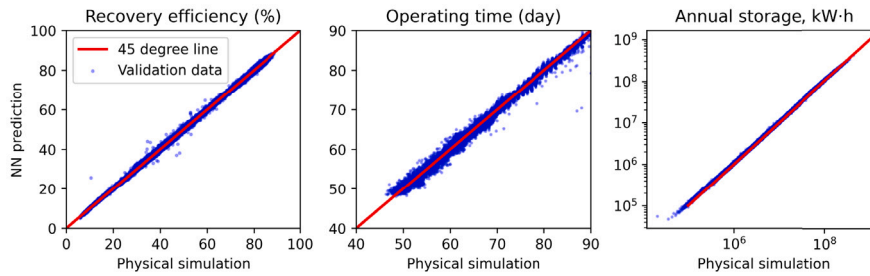
(c) Seasonal cycle scenario - cross validation

(d) Seasonal cycle scenario- relative error

Fig. 8. (a, c) Cross-validation of the two multi-layer neural network models between the physical simulation results and the neural network predictions using the testing data set. (b, d) Histogram of relative absolute error for the two neural networks in the testing data set. The averages of absolute relative error are $3.3\%, 1.1\%$, 2.0% and 0.2% for the performance metrics of the continuous operation scenario and $0.6\%, 0.4\%$, and 0.1% for the performance metrics of the seasonal cycle scenario.

are $3.3\%, 1.1\%, 2\%$, and 0.2% respectively for the performance metrics. While for the seasonal cycle operation, about $60\%, 70\%$, and 99% of all test data have an error less than 1% for the recovery efficiency, charging time, and annual storage, respectively. And the averages of the absolute relative error are $0.6\%, 0.4\%$, and 0.1% respectively for the performance metrics. The statistical analysis further validates that the trained ANN model of the seasonal cycle operation has better accuracy than the trained model of the continuous operation. The $\leq 3.3\%$ error

for all performance metrics of both operations indicates that the ANN models effectively adapt to the data structure.

3.2. Site operation optimization

Site suitability investigation is usually conducted by comparing recovery efficiency for various operation conditions [4,11]. We demonstrate the application of the trained ANN models in the multi-objective

Table 4
Formation characteristics from literature of four potential sites for RTES. Note we ignore the heterogeneity and calculated the average values for all sites.

Formation	Permeability $\kappa(m^2)$	Porosity $n(-)$	T. Conductivity $\lambda(W/(m_K))$	Depth Z (m)	Thickness H (m)
Mt. Simon [53]	1.1E–13	0.161	4.2	1750	137
Weber Sandstone [54–58]	3.0E–14	0.100	3.3	3000	100
St. Peter [53]	1.6E–13	0.167	3.3	610	59
L. Tuscaloosa [51,52]	8.9E–14	0.310	3.3	3200	24

optimization algorithm (Section 2.4) to quickly and comprehensively co-evaluate the multi-performance metrics of any given site in the multi-dimensional operational parametric space. Table 4 lists the four potential RTES sites with formation characteristics collected from the literature. The Mt. Simon Sandstone and St. Peter Sandstone are located in the Illinois Basin and have been extensively characterized for CO_2 storage [47] and gas storage [48]. The Weber Sandstone of the Green River Basin in Wyoming was thoroughly evaluated as a target CO_2 reservoir for the Wyoming Carbon Underground Project [49], and the Lower Tuscaloosa Sandstone of the Gulf Coast Basin in SW Mississippi was evaluated and tested by the Southeast Regional Carbon Sequestration Partnership for storing CO_2 in deep depleted oil fields [50–52]. The availability of formation characteristics from past investigations and the high porosity and permeability make all four sites potentially suitable candidates for HT-RTES.

Note, the data listed in Table 4 are average values to satisfy the assumptions made in the stochastic realization of the physics-based simulations. This may bring an inaccurate representation of the actual reservoir conditions, for example, the reservoir pore pressure and temperature may not follow the relation in Eqs. (4) and (5). However, we argue that the application of ANN models in this paper is designed for the early stage of RTES planning for site suitability evaluation. Once a specific site is chosen, machine learning can be applied to accelerate the physics-based simulation to generate grid-scale results using detailed formation characteristics [30], which is beyond the scope of this paper. The formation characteristics of the four sites show similar permeability, porosity, and thermal conductivity, yet, the depth and thickness show significant variation. In addition, the formation thickness of the Mt. Simon and the depth of the Lower Tuscaloosa slightly exceed the limitation of the stochastic data range. However, the ANN models can still predict RTES performance with an acceptable error by extrapolating the data pattern from their training, as we validated the extrapolation by comparing ANN predictions against physics-based simulations for the two sites with various operations. The extrapolation of ANN models outside of their training domain has been practiced in CO_2 sequestration [59] and heat transfer [60]. Note the ranges given in Table 1 cover most sites that are technically and economically suitable for RTES. In order to avoid hydrofracturing the formation and the unreasonable charging time, we restrain the injection rate as $1 \leq \log(Q) \leq 3$ for the Mt. Simon and Weber sandstones, and $0.1 \leq \log(Q) \leq 1$ for the St. Peter and Lower Tuscaloosa sandstones using the Theis theory with the listed formation characteristics in Table 4.

Fig. 9(a) and Fig. 9(b) show the ANN models' predicted response of RTES performance in the 3-dimensional operational space(i.e., injection fluid temperature T_i, injection rate Q, and well distance D) for the continuous operation and the seasonal cycle scenarios of the Weber Sandstone formation, respectively. We can see the optimal solutions for each performance metric are different within the same operation. For example, the solution of maximum recovery efficiency for continuous operation (Fig. 9(a)) is located at low injection temperature and injection rate with a long well distance, yet, the maximum storage capacity requires high injection temperature. We can also observe that the optimal solution for the same performance metrics (e.g., recovery efficiency) is different between different operation scenarios. For example, the optimal recovery efficiency for the continuous operation

(Fig. 9(a)) is realized with low injection temperature. In contrast, the maximum recovery efficiency for the seasonal cycle (Fig. 9(b)) requires high injection temperature. These differences suggest the performance metrics have competing optimal solutions. We use the genetic algorithm described in Section 2.4 to generate Pareto fronts of the multiple objectives (i.e., performance metrics).

Fig. 10 shows the calculated Pareto fronts of the RTES performance metrics for the four potential sites. The charging time, operating time, and storage capacity of the continuous operation in Fig. 10(a) and the annual storage of the seasonal cycle in Fig. 10(b) are in log scale, in correspondence to the training data set. We tested the influence of the genetic algorithm parameters on the Pareto solution. A higher number of the initial population or a higher number of maximum generation results in the same solution as before, indicating the validity of the Pareto fronts in Fig. 10. We underline that the constraints from formation parameters make the surrogate ANN models site-dependent and lead to different viable solution, which results in different shapes (curves or surfaces) of the Pareto fronts if three or more objectives are co-optimized together. Instead, we co-optimize only two RTES performance metrics per time (e.g., recovery efficiency and operating time shown in the second sub-figure of Fig. 10(a)) and ignore the rest of the performance metrics. As a result, we have 3 and 2 Pareto fronts for the continuous operation and the seasonal cycle scenarios, respectively.

Fig. 10(a) shows that the computed optimal recovery efficiency is competing against the charging time, the operating time, and the storage capacity for all formations of the continuous operational scenario. Note, the objectives are to minimize charging time while maximizing the rest of the metrics. The St. Peter sandstone (blue lines) has the lowest range of recovery efficiency among the four formations, which makes it the least favorable for HT-RTES. This low recovery efficiency is primary because the low initial formation temperature, which is linearly correlated with formation depth (Eq. (5)), causes significant heat loss. The Mt. Simon sandstone (black lines) can achieve a maximum 45% recovery efficiency, at which it can only operate for about 15 days with a storage capacity of about 1.5E8 kW·h. The buoyancy effect with large formation thickness results in an intermediate recovery efficiency. The Weber sandstone (red lines) and the L. Tuscaloosa sandstone (green lines) can reach about 65% recovery efficiency with around 100 days of charging time. However, the Weber Sandstone has better storage capacity than the L. Tuscaloosa formation due its higher formation thickness. With the above reasoning, we find that the Weber Sandstone (red lines) has a balanced performance over all the targeted metrics.

Fig. 10(b) shows the predicted Pareto fronts among the three performance metrics of the seasonal cycle scenario. Comparing the ranges of the optimal solutions against the results of the continuous operation scenario, each site has a different response. For example, the St. Peter Sandstone has a recovery efficiency in the range of 10%–25% for the continuous operation scenario (blue line in Fig. 10(a)-II), yet, this range increases to 53% for the seasonal cycle scenario (blue line in Fig. 10(b)-I). This indicates the performance of RTES is operation scenario dependent. We define the trade-off factor as the absolute derivative of object 1 (e.g., operating time) over object 2 (e.g., recovery efficiency), i.e., the slope of Pareto lines. We find that the trade-off factors are close to each other, which indicates the rate of sacrificing operating time for recovery efficiency (annual storage) gain is similar for all formations except for the St. Peter Sandstone. The St. Peter Sandstone has very narrow ranges for all performance metrics (magnified as subplots at the right of Fig. 10(b)) because of its low and narrow range of injection rate, shallow depth, and small thickness. For the seasonal cycle scenario, the Mt. Simon Sandstone and the Weber Sandstone have close and superior performance over the other two sites as the Pareto fronts of the two sites are close to each other and have higher ranges in all targeted performance metrics.
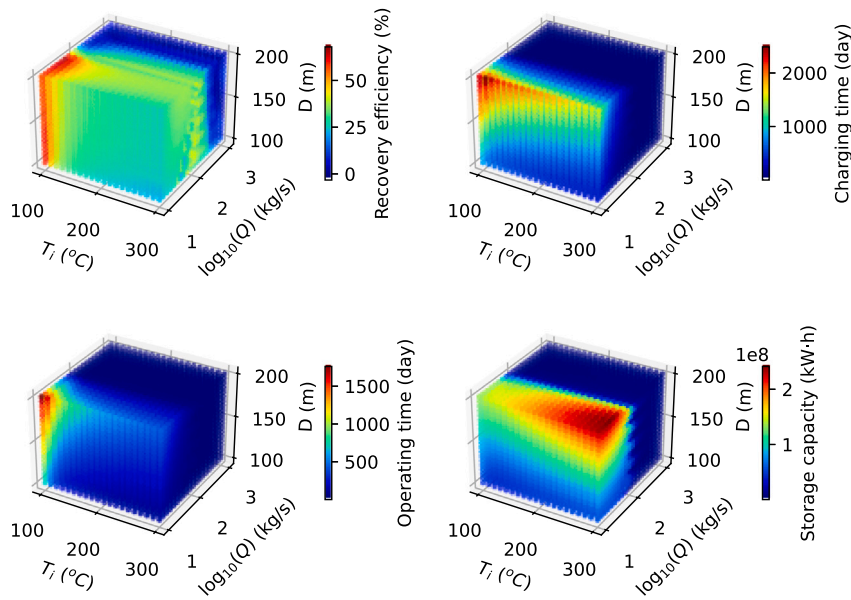
(a) Continuous operation scenario
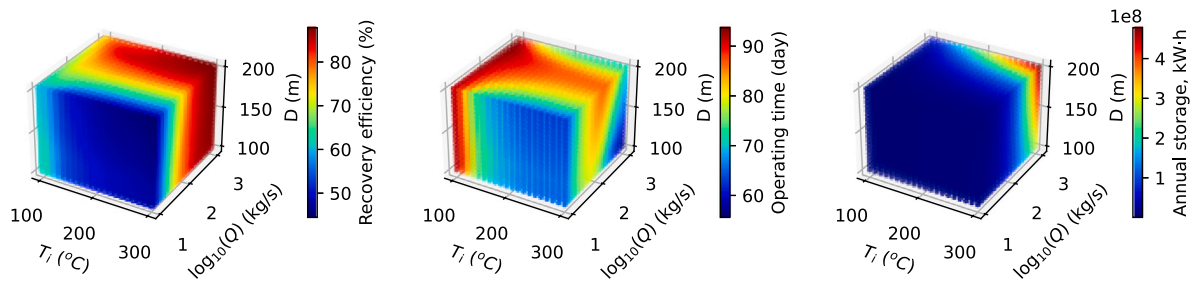
(b) Seasonal cycle scenario

Fig. 9. Weber sandstone HT-RTES performance responses in the space of operation. T_i is fluid injection temperature, Q represents injection rate (in log-scale), and D is well distance.

4. Discussion

This study utilizes a big data set synthesized from physics-based simulations and demonstrates the effectiveness and computational efficiency of using the machine learning method for RTES site evaluation. For example, a single physics-based simulation takes about 3 h to finish on a cluster node with 24 cores for a given site with a fixed operation, and it will take 3000 h to generate the 3D performance matrix response shown in Fig. 9, if the Latin hypercube sampling was used to sample 10 values from each distribution of the 3 operational conditions. With the trained ANN models, the generation of the 3D responses shown in Fig. 9 was completed in a fraction of a second. We admit the data set generation is computationally expensive, and we approximately spent two weeks obtaining the training and testing data set for each operating scenario with a fixed formation thickness using 1000 computational cores. This is affordable with access to high-performance computing resources. However, the reduced-order ANN models trained by this data set can be used to investigate any formations with parameters within or slightly exceeding the ranges listed in Table 1. Also, the trained ANN models can be used by all stakeholders with basic knowledge of Python and a few lines of coding, instead of a professional who needs to be well trained on the numerical method and the physical processes.

ANN model performance highly depends on the handling of the data set. Data set with each variable of the stochastic input and the performance metrics having a close to uniform or normal distribution results in a more accurate ANN model. Take the annual storage of the seasonal cycle as an example, its value ranges several magnitudes with an exponential distribution of the histogram. The direct training with this data set results in an average absolute relative error of about 9%. We transformed the data set in logarithmic scale, which turned it into a close to normal distribution shown in Fig. 6(b). With the transformed data set, the newly trained ANN model can accurately predict annual storage with an average absolute relative error of 0.1% shown in Fig. 8(d). Consequently, we transformed the charging time, operating time, and storage capacity of the continuous operation using logarithmic scales.

The Pareto fronts shown in Fig. 10 provide a design tool for engineers and decision-makers to select the RTES site most suitable for a particular operation scenario (fluid cycle), and also to estimate the best practice in terms of RTES operation parameters. Once a specific site has been chosen, a suite of physics-based simulations with detailed formation characteristics needs to be run with stochastic operation parameters. Machine learning algorithms can be directly used to predict the unknown variables of the partial differential equations (PDE) at the discrete grids, which has been adopted in the simulation of CO_2 sequestration [30,59]. Following the proposed method, these machine learning accelerated models can be combined with objective optimization algorithms, like the genetic algorithms adopted in this paper, to
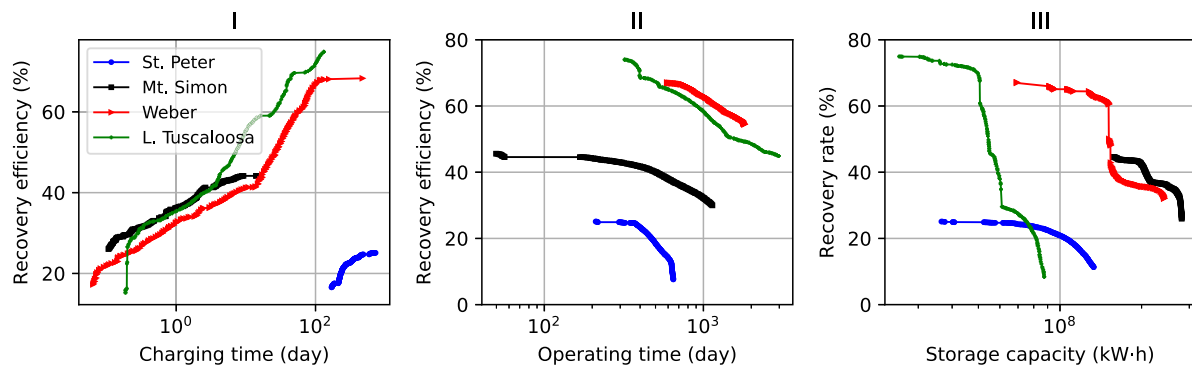
(a) Continuous operation scenario
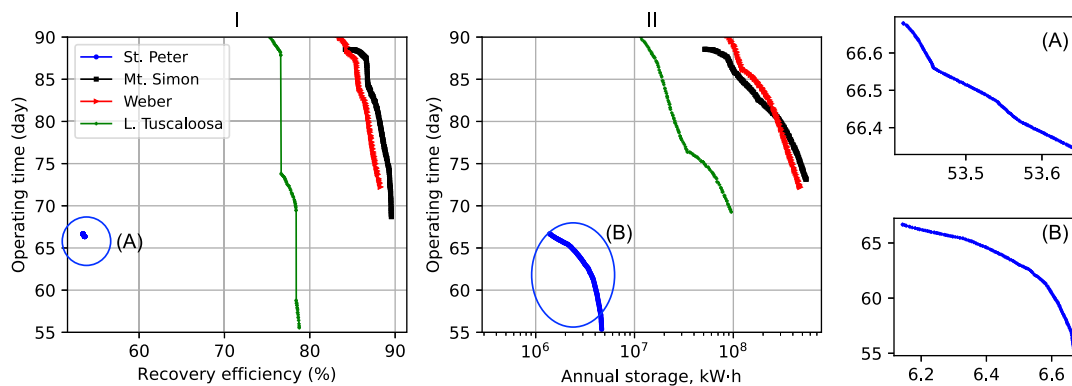
(b) Seasonal cycle scenario

Fig. 10. Comparison of the multi-objective Pareto fronts for the identified four sites using the validated neural network model and a genetic optimization algorithm. The genetic algorithm produces points along the Pareto front, and we connect those points to present the Pareto front.

generate Pareto fronts from which stakeholders can choose the best combination of operating parameters. In addition, the operation in terms of fluid injection rate and fluid injection temperature can be adjusted to yield optimal performance of the Pareto front during RTES operation.

5. Conclusions

This work proposes a methodology to optimize high-temperature reservoir thermal energy storage (RTES) by the combination of physics-based thermo-hydraulic (TH) simulation, artificial neural network (ANN) surrogate model development, and genetic algorithm-based multi-objective optimization. With the help of automated input variable sampling from their corresponding stochastic distribution, the physics-based simulations generate big data with formation characteristics and operation conditions as input, and RTES performance metrics as output, for a doublet well configuration with two operational scenarios: continuous operation and seasonal cycles. These data are then used to train and validate two deep-layer ANN models with architectures optimized by the Bayesian search algorithm. Serving as the surrogate models, the ANN models are used in combination with a genetic algorithm to search the space of operational conditions constrained by the formation characteristics of four potential RTES sites. The responses for each performance metric and the Pareto fronts of two competing performance metrics show that the RTES performance is operational scenario (i.e., fluid cycle) and site-dependent and the metrics have a competing effect. We conclude that there is not a single optimal site for RTES and there is not a single optimal solution for operating a

specific site. The established methodology brings new insight in RTES, as well as all other engineering optimization problems with multiple objectives. The trained ANN models can be used to quickly screen potential formations for HT-RTES, provided the five formation characteristics (i.e., permeability, porosity, thermal conductivity, depth, and thickness) fall in the investigated ranges.

The above conclusion and the developed neural network models are based on the assumption that the mechanical deformation and geochemical reaction effects are not significant and the formation's physical properties are isotropic and homogeneous. As indicated by the authors' recent paper [61], these mechanisms and factors will have an influence on the performance and longevity of the RTES system. The proposed workflow is challenged to develop neural network models as too many variables are involved in mechanics, fluid chemistry, and rock mineralogy and we cannot generate enough training data even with HPC resources. Future work will be dedicated to developing neural network models to predict RTES performance with arbitrary operations for a specific site considering the fully coupled thermo–hydro–mechano–chemical processes with formation heterogeneity.

CRediT authorship contribution statement

Wencheng Jin: Conceptualization, Investigation, Methodology, Data analysis, Original draft and editing. **Trevor A. Atkinson:** Geological data collection, Writing – review & editing. **Christine Doughty:** Writing – review & editing. **Ghanashyam Neupane:** Writing – review & editing. **Nicolas Spycher:** Writing – review &

References

[1] P. Denholm, M. O'Connell, G. Brinkman, J. Jorgenson, Overgeneration from solar energy in California. a field guide to the duck chart, Tech. rep., National Renewable Energy Lab.(NREL), Golden, CO (United States), 2015, http://dx.doi.org/10.2172/1226167.

[2] S. Green, J. McLennan, P. Panja, K. Kitz, R. Allis, J. Moore, Geothermal battery energy storage, Renew. Energy 164 (2021) 777–790, http://dx.doi.org/10.1016/j.renene.2020.09.083.

[3] B. Drijver, M. van Aarssen, B. de Zwart, High-temperature aquifer thermal energy storage (HT-ATES): sustainable and multi-usable, in: Innostock 2012-12th International Conference on Energy Storage, 2012, p. 10.

[4] H.A. Sheldon, A. Wilkins, C.P. Green, Recovery efficiency in high-temperature aquifer thermal energy storage systems, Geothermics 96 (2021) 102173, http://dx.doi.org/10.1016/j.geothermics.2021.102173.

[5] P. Fleuchaus, B. Godschalk, I. Stober, P. Blum, Worldwide application of aquifer thermal energy storage – a review, Renew. Sustain. Energy Rev. 94 (2018) 861–876, http://dx.doi.org/10.1016/j.rser.2018.06.057.

[6] R.M. Zeghici, A. Damian, R. Frunzulic, F. Iordache, Energy performance assessment of a complex district heating system which uses gas-driven combined heat and power, heat pumps and high temperature aquifer thermal energy storage, Energy Build. 84 (2014) 142–151, http://dx.doi.org/10.1016/j.enbuild.2014.07.061.

[7] X. Shi, S. Jiang, H. Xu, F. Jiang, Z. He, J. Wu, The effects of artificial recharge of groundwater on controlling land subsidence and its influence on groundwater quality and aquifer energy storage in Shanghai, China, Environ. Earth Sci. 75 (3) (2016) 195, http://dx.doi.org/10.1007/s12665-015-5019-x.

[8] F.J. Molz, J.C. Warman, T.E. Jones, Aquifer storage of heated water: Part I — A field experiment, Groundwater 16 (4) (1978) 234–241, http://dx.doi.org/10.1111/j.1745-6584.1978.tb03230.x.

[9] F.J. Molz, A.D. Parr, P.F. Andersen, V.D. Lucido, J.C. Warman, Thermal energy storage in a confined aquifer: Experimental results, Water Resour. Res. 15 (6) (1979) 1509–1514, http://dx.doi.org/10.1029/WR015i006p01509.

[10] M. Gutierrez-Neri, N. Buik, B. Drijver, Analysis of recovery efficiency in a high-temperature energy storage system, 2011, p. 4.

[11] G. Schout, B. Drijver, M. Gutierrez-Neri, R. Schotting, Analysis of recovery efficiency in high-temperature aquifer thermal energy storage: a Rayleigh-based method, Hydrogeol. J. 22 (1) (2014) 281–291, http://dx.doi.org/10.1007/s10040-013-1050-8.

[12] L. Gao, J. Zhao, Q. An, X. Liu, Y. Du, Thermal performance of medium-to-high-temperature aquifer thermal energy storage systems, Appl. Therm. Eng. 146 (2019) 898–909, http://dx.doi.org/10.1016/j.applthermaleng.2018.09.104.

[13] J.W. Tholen, Potential for High Temperature-Aquifer Thermal Energy Storage (HT-ATES) in the Dutch subsurface, Utrecht University, 2017, Accepted: 2018-05-22T17:01:01Z.

[14] T. Wegman, HT-ATES system case study on TU Delft campus: Increasing efficiency with density difference compensation with the application of saline groundwater from deeper layers, Delft University of Technology, 2017.

[15] G. Winterleitner, F. Schütz, C. Wenzlaff, E. Huenges, The impact of reservoir heterogeneities on high-temperature aquifer thermal energy storage systems. a case study from northern Oman, Geothermics 74 (2018) 150–162, http://dx.doi.org/10.1016/j.geothermics.2018.02.005.

[16] C. Doughty, G. Hellström, C.F. Tsang, J. Claesson, A dimensionless parameter approach to the thermal behavior of an aquifer thermal energy storage system, Water Resour. Res. 18 (3) (1982) 571–587, http://dx.doi.org/10.1029/WR018i003p00571.

[17] J. Kim, Y. Lee, W.S. Yoon, J.S. Jeon, M.-H. Koo, Y. Keehm, Numerical modeling of aquifer thermal energy storage system, Energy 35 (12) (2010) 4955–4965, http://dx.doi.org/10.1016/j.energy.2010.08.029.

[18] A. Yapparova, S. Matthäi, T. Driesner, Realistic simulation of an aquifer thermal energy storage: Effects of injection temperature, well placement and groundwater flow, Energy 76 (2014) 1011–1018, http://dx.doi.org/10.1016/j.energy.2014.09.018.

[19] W. Jin, R. Podgorney, T. McLing, THM coupled numerical analysis on the geothermal energy storage & extraction in porous fractured reservoir, in: 54th US Rock Mechanics/Geomechanics Symposium, OnePetro, 2020.

[20] P. Fleuchaus, S. Schüppler, M. Bloemendal, L. Guglielmetti, O. Opel, P. Blum, Risk analysis of high-temperature aquifer thermal energy storage (HT-ATES), Renew. Sustain. Energy Rev. 133 (2020) 110153, http://dx.doi.org/10.1016/j.rser.2020.110153.

[21] D.M. Ginosar, D.S. Wendt, Metrics for the Evaluation of Reservoir Thermal Energy Storage, Tech. rep., Idaho National Laboratory, 2020.

[22] W. Jin, R. Podgorney, T. McLing, R. Carlsen, Geothermal battery optimization using stochastic hydro-thermal simulations and machine learning algorithms, in: 55th US Rock Mechanics/Geomechanics Symposium, OnePetro, 2021.

[23] K.J. Bergen, P.A. Johnson, V. Maarten, G.C. Beroza, Machine learning for data-driven discovery in solid earth geoscience, Science 363 (6433) (2019) http://dx.doi.org/10.1126/science.aau0323.

[24] M. Valera, Z. Guo, P. Kelly, S. Matz, V.A. Cantu, A.G. Percus, J.D. Hyman, G. Srinivasan, H.S. Viswanathan, Machine learning for graph-based representations of three-dimensional discrete fracture networks, Comput. Geosci. 22 (3) (2018) 695–710, http://dx.doi.org/10.1007/s10596-018-9720-1.

[25] S. Srinivasan, S. Karra, J. Hyman, H. Viswanathan, G. Srinivasan, Model reduction for fractured porous media: a machine learning approach for identifying main flow pathways, Comput. Geosci. 23 (3) (2019) 617–629, http://dx.doi.org/10.1007/s10596-019-9811-7.

[26] J. Wu, X. Yin, H. Xiao, Seeing permeability from images: fast prediction with convolutional neural networks, Sci. Bull. 63 (18) (2018) 1215–1222, http://dx.doi.org/10.1016/j.scib.2018.08.006.

[27] A. Rabbani, M. Babaei, Image-based modeling of carbon storage in fractured organic-rich shale with deep learning acceleration, Fuel 299 (2021) 120795, http://dx.doi.org/10.1016/j.fuel.2021.120795.

[28] B. Chen, D.R. Harp, Y. Lin, E.H. Keating, R.J. Pawar, Geologic CO2 sequestration monitoring design: A machine learning and uncertainty quantification based approach, Appl. Energy 225 (2018) 332–345, http://dx.doi.org/10.1016/j.apenergy.2018.05.044.

[29] J. You, W. Ampomah, Q. Sun, Co-optimizing water-alternating-carbon dioxide injection projects using a machine learning assisted computational framework, Appl. Energy 279 (2020) 115695, http://dx.doi.org/10.1016/j.apenergy.2020.115695.

[30] H. Wu, N. Lubbers, H.S. Viswanathan, R.M. Pollyea, A multi-dimensional parametric study of variability in multi-phase flow dynamics during geologic CO2 sequestration accelerated with machine learning, Appl. Energy 287 (2021) 116580, http://dx.doi.org/10.1016/j.apenergy.2021.116580.

[31] R. Podgorney, H. Huang, C. Lu, D. Gaston, C. Permann, L. Guo, D. Andrs, Falcon: a Physics-based and Massively Parallel and Fully-Coupled, Finite Element Model for Simultaneously Solving Multiphase Fluid Flow, Heat Transport, and Rock Deformation for Geothermal Reservoir Simulation, Tech. Rep., (INL/EXT-11e23351) Idaho National Laboratory, 2014.

[32] Y. Xia, R. Podgorney, Falcon: Finite element geothermal reservoir simulation code, 2015, URL https://github.com/idaholab/.

[33] C.J. Permann, D.R. Gaston, D. Andrš, R.W. Carlsen, F. Kong, A.D. Lindsay, J.M. Miller, J.W. Peterson, A.E. Slaughter, R.H. Stogner, et al., MOOSE: Enabling massively parallel multiphysics simulation, SoftwareX 11 (2020) 100430, http://dx.doi.org/10.1016/j.softx.2020.100430.

[34] A. Tinni, E. Fathi, R. Agarwal, C. Sondergeld, Y. Akkutlu, C. Rai, Shale permeability measurements on plugs and crushed samples, in: SPE Canadian Unconventional Resources Conference, OnePetro, 2012, http://dx.doi.org/10.2118/162235-MS.

[35] B. Ermagambet, B. Kasenov, N. Nurgaliyev, M. Nabiev, Z.M. Kasenova, M. Kazankapova, A. Zikirina, Electrophysical properties and heat capacity of shale from the Kendyrlyk deposit, Solid Fuel Chem. 52 (2) (2018) 138–141, http://dx.doi.org/10.3103/S0361521918020039.

[36] H. Wen, J.-h. Lu, Y. Xiao, J. Deng, Temperature dependence of thermal conductivity, diffusion and specific heat capacity for coal and rocks from coalfield, Thermochim. Acta 619 (2015) 41–47, http://dx.doi.org/10.1016/j.tca.2015.09.018.

[37] J.-J. Dong, J.-Y. Hsu, W.-J. Wu, T. Shimamoto, J.-H. Hung, E.-C. Yeh, Y.-H. Wu, H. Sone, Stress-dependence of the permeability and porosity of sandstone and shale from TCDP hole-a, Int. J. Rock Mech. Min. Sci. 47 (7) (2010) 1141–1157, http://dx.doi.org/10.1016/j.ijrmms.2010.06.019.

[38] J.J. Zhang, Applied Petroleum Geomechanics, Gulf Professional Publishing, 2019.

[39] W. Dowdle, W. Cobb, Static formation temperature from well logs-an empirical method, J. Pet. Technol. 27 (11) (1975) 1326–1330, http://dx.doi.org/10.2118/5036-PA.

[40] W. Wagner, J. Cooper, A. Dittmann, J. Kilima, H. Kretzschmar, A. Kruse, R. Mares, K. Oguchi, H. Sato, I. Stocker, et al., The IAPWS industrial formulation 1997 for the thermodynamic properties of water and steam, Trans. ASME-A-Eng. Gas Turbines Power 122 (1) (2000) 150, http://dx.doi.org/10.1115/1.483186.

[41] A. Wilkins, C.P. Green, J. Ennis-King, PorousFlow: a multiphysics simulation code for coupled problems in porous media, J. Open Source Softw. 5 (55) (2020) 2176, http://dx.doi.org/10.21105/joss.02176.

[42] C.V. Theis, The relation between the lowering of the piezometric surface and the rate and duration of discharge of a well using groundwater storage, EOS, Trans. Am. Geophys. Union 16 (2) (1935) 519–524, http://dx.doi.org/10.1029/TR016i002p00519.

[43] J. Snoek, H. Larochelle, R.P. Adams, Practical bayesian optimization of machine learning algorithms, Adv. Neural Inf. Process. Syst. 25 (2012) http://dx.doi.org/10.48550/arXiv.1206.2944.

[44] D.P. Kingma, J. Ba, Adam: A method for stochastic optimization, 2014, arXiv preprint arXiv:1412.6980.

[45] Jazzbin, et al., Geatpy: The genetic and evolutionary algorithm toolbox with high performance in Python, 2020.

[46] K. Deb, A. Pratap, S. Agarwal, T. Meyarivan, A fast and elitist multiobjective genetic algorithm: NSGA-II, IEEE Trans. Evol. Comput. 6 (2) (2002) 182–197, http://dx.doi.org/10.1109/4235.996017.

[47] R.J. Finley, S.E. Greenberg, S.M. Frailey, I.G. Krapac, H.E. Leetaru, S. Marsteller, The path to a successful one-million tonne demonstration of geological sequestration: Characterization, cooperation, and collaboration, Energy Procedia 4 (2011) 4770–4776, http://dx.doi.org/10.1016/j.egypro.2011.02.441.

[48] A. Stumpf, J. Damico, et al., Feasibility of a deep direct-use geothermal system at the university of illinois Urbana-champaign, GRC Trans. 42 (DOE-UIUC-08106) (2018) http://dx.doi.org/10.15121/1495413.

[49] R.C. Surdam, Geological CO2 Storage Characterization: The Key to Deploying Clean Fossil Energy Technology, Springer Science & Business Media, 2013, http://dx.doi.org/10.1007/978-1-4614-5788-6.

[50] C. Doughty, B.M. Freifeld, Modeling CO2 injection at cranfield, mississippi: Investigation of methane and temperature effects, Greenh. Gases: Sci. Technol. 3 (6) (2013) 475–490, http://dx.doi.org/10.1002/ghg.1363.

[51] S. Kim, S.A. Hosseini, Above-zone pressure monitoring and geomechanical analyses for a field-scale CO2 injection project in cranfield, MS, Greenh. Gases: Sci. Technol. 4 (1) (2014) 81–98, http://dx.doi.org/10.1002/ghg.1388.

[52] H. Jung, D.N. Espinoza, Chemo-poromechanical properties of Tuscaloosa sandstone: Implications on CO2 geological storage, in: 51st US Rock Mechanics/Geomechanics Symposium, OnePetro, 2017.

[53] J. Damico, Geocellular Model of Mt. Simon Sandstone for University of Illinois at Urbana-Champaign DDU feasibility study, Tech. rep., DOE Geothermal Data Repository; Univ. of Illinois at Urbana-Champaign, IL, 2018, http://dx.doi.org/10.15121/1495417.

[54] E.A. Johnson, Geologic assessment of undiscovered oil and gas resources in the Phosphoria total petroleum system, southwestern Wyoming province, Wyoming, Colorado, and Utah, in: National Assessment of Oil and Gas Project- Petroleum Systems and Geologic Assessment of Oil and Gas in the Southwestern Province, Wyoming, Colorado, and Utah, U.S. Geological Survey, 2005, http://dx.doi.org/10.3133/ds69D.

[55] H. Deng, P.H. Stauffer, Z. Dai, Z. Jiao, R.C. Surdam, Simulation of industrial-scale CO2 storage: Multi-scale heterogeneity and its impacts on storage capacity, injectivity and leakage, Int. J. Greenh. Gas Control 10 (2012) 397–418, http://dx.doi.org/10.1016/j.ijggc.2012.07.003.

[56] J.F. McLaughlin, M. Garcia-Gonzalez, Detailed geologic characterization of core and well data from the Weber and Madison formations and associated seals at a potential CO2 sequestration site in southwest Wyoming: Definining the Lithologic, geochemical, diagenetic, and burial histories relative to successful CO2 storage, in: Geological CO2 Storage Characterization, Springer, 2013, pp. 55–96, http://dx.doi.org/10.1007/978-1-4614-5788-6_6.

[57] E. Robertson, Thermal properties of rocks, USgs open file report 88-441, US geological, in: Survey, U.S. Geological Survey, Reston, Va, 1988, p. 70, http://dx.doi.org/10.3133/ofr88441.

[58] L.R. Shafer, Assessing Injection Zone Fracture Permeability Through Identification of Critically Stressed Fracture Orientations At the Rock Springs Uplift CO2 Sequestration Site, SW Wyoming, University of Wyoming, 2013.

[59] G. Wen, M. Tang, S.M. Benson, Towards a predictor for CO2 plume migration using deep neural networks, Int. J. Greenh. Gas Control 105 (2021) 103223, http://dx.doi.org/10.1016/j.ijggc.2020.103223.

[60] Y. Liu, N. Dinh, Y. Sato, B. Niceno, Data-driven modeling for boiling heat transfer: using deep neural networks and high-fidelity simulation results, Appl. Thermal Eng. 144 (2018) 305–320, http://dx.doi.org/10.1016/j.applthermaleng.2018.08.041.

[61] W. Jin, T. Atkinson, G. Neupane, T. McLing, C. Doughty, N. Spycher, P. Dobson, R. Smith, Influence of mechanical deformation and mineral dissolution/precipitation on reservoir thermal energy storage, in: 56th US Rock Mechanics/Geomechanics Symposium, OnePetro, 2022.